

Cart3D Simulations for the First AIAA Sonic Boom Prediction Workshop

Michael J. Aftosmis*

NASA Ames, Moffett Field, CA 94035

Marian Nemec†

Science & Technology Corp., Moffett Field, CA 94035

Simulation results for the First AIAA Sonic Boom Prediction Workshop are presented using an inviscid, embedded-boundary Cartesian mesh method. The method employs adjoint-based error estimation and adaptive meshing to automatically determine resolution requirements for each simulation. Results are presented for both mandatory and optional test cases. These include a low-boom body of revolution, a 69° delta wing model and a model of the Lockheed supersonic tri-jet with V-tail and flow-through nacelles. In addition to signature data, each example includes an assessment of mesh independence of the near- and mid-field pressure signatures. We also show mesh convergence of the adaptation functional and demonstrate that both the adjoint correction and remaining error are vanishing as the mesh is refined. Data provided include both the pressure signals required by the workshop and information on code performance in terms of processing time and memory usage. In addition, the discussion demonstrates useful techniques for prediction of extreme off-track pressure signatures and an adjoint-based technique for tracing features of the off-body pressure signature back to specific portions of the geometry and flow field.

Nomenclature

h	Altitude above sensor at model nose/apex	α	Angle of attack
\mathcal{J}	Scalar functional or output of interest	β	Sideslip angle
L	Reference length	Φ	Off-track angle ("On-track" at $\Phi = 0^\circ$)
h/L	Non-dimensional distance to sensor	σ	Standard deviation
p	Local static pressure	$R(\cdot)$	Residual of the discretization
M	Mach number	$(\cdot)_H$	Values on mesh with cell size H
Q	State vector of conserved variables	$(\cdot)_\infty$	Free stream conditions
w_i	Weight of i^{th} component of the functional, \mathcal{J}_i		

I. Introduction

ANALYSIS methods for sonic-boom prediction have improved dramatically in recent years as a result of both commercial and government interest in overland supersonic flight. Backed by programmatic investment within NASA and the aerospace community, a number of simulation tools have recently become available for predicting high-fidelity pressure signals several body lengths away from an aircraft.^{1–11} At such distances, details of the three-dimensional aircraft geometry become less important and atmospheric propagation codes^{12–14} then model wave propagation through the atmosphere and to the ground.

While several technologies have played roles in improving the effectiveness of CFD-based analysis, one of the keys has been the widespread use of adaptive mesh techniques.^{1–4, 6, 7, 15–17} By design, low sonic-boom vehicles send only weak pressure disturbances toward the ground. Accurate propagation of these weak waves over several body lengths is a challenge for any numerical simulation technique. Adaptive meshing techniques concentrate and orient mesh elements in the computational domain to more efficiently propagate these signals and have been far more successful than earlier efforts. Particularly noteworthy has been the contribution of adjoint weighted or output-based meshing approaches, which can prioritize mesh refinement specifically to reduce error in the propagated signal.^{3, 4, 6, 16, 18} The insight provided by these methods has

*Aerospace Engineer. Applied Modeling & Simulation Branch. michael.aftosmis@nasa.gov, Associate Fellow AIAA.

†Senior Research Scientist. Applied Modeling & Simulation Branch. marian.nemec@nasa.gov, Member AIAA.

benefitted even fixed-mesh approaches since they aid in our understanding of flow sensitivities, meshing requirements and the role of discretization error throughout the flow field.

The objective of the first sonic-boom prediction workshop is to document the state of the art for prediction of near-field pressure signatures and gain an understanding of modeling requirements for accurate and reliable sonic boom prediction.¹⁹ To facilitate direct comparison, the workshop organizers provide both CAD geometry as well as surface and volume grids for structured, unstructured (tetrahedral) and mixed-element grids. Workshop participants were requested to apply their best practices for computing solution on the provided geometries. In addition, there was particular interest in exploring refinement techniques including grid adaptation and alignment with flow characteristics.

Although embedded-boundary Cartesian grids are used quite broadly within the low-boom design community, Cartesian meshes were not included in the grid-sets provided by the organizing committee. Cartesian methods have been of interest since at least the 2008 NASA Fundamental Aeronautics Low Boom Workshop²⁰ and many of the specialized techniques commonly used for such computations were pioneered on these grids.⁴ While Cartesian grids were not distributed *per se*, surface representations (either CAD or unstructured surface triangulations) were included, and these provided the geometric models for this work. Meshes used in this work were chosen to roughly correspond to the resolution levels provided for other simulation techniques considered by the workshop organizers for the various problems.

II. Background and Numerical Method

In early 2008, Nemec, Aftosmis and Wintzer³ used embedded-boundary Cartesian meshing along with adjoint-based mesh adaptation to predict the pressure signature generated by a diamond airfoil in supersonic flow. This work used an off-body functional to drive the adjoint and introduced a mesh alignment technique based on the Mach-angle of the free-stream flow. The capability was built upon a preexisting mesh adaptation scheme and adjoint solver.^{21,22} Three dimensional examples using the Cartesian-adjoint approach for boom prediction were presented in June 2008⁴ and the method was subsequently used to participate in the 2008 NASA Fundamental Aeronautics Program Sonic Boom Prediction Workshop.²⁰

The Cart3D simulation package uses a Cartesian cut-cell approach²³ in which the Euler equations are discretized on a multilevel Cartesian mesh with embedded boundaries. The mesh consists of regular Cartesian hexahedra everywhere, except for a layer of body-intersecting cells at boundaries as illustrated in Figure 2. The spatial discretization uses a second-order accurate finite volume method with a weak imposition of boundary conditions, resulting in a system of equations with the form

$$R(Q_H) = 0 \quad (1)$$

where $R(\cdot)$ is the residual operator of the discretization and Q_H is the state vector on the current mesh.

The flux-vector splitting approach of van Leer²⁴ is used for residual evaluation. Although the mesh consists of nested Cartesian cells, it is viewed as an unstructured collection of control volumes making the approach well-suited for solution-adaptive mesh refinement. Steady-state flow solutions are obtained using a five-stage Runge-Kutta scheme with local time stepping and multigrid. Domain decomposition via space-filling curves permits parallel computation; for more details see Aftosmis *et al.* and Berger *et al.*^{25–27}

When applied to boom propagation problems, the Cartesian mesh is frequently rotated to roughly align the mesh cells with the free stream Mach-wave angle. This alignment also enables cell stretching along the dominant wave propagation direction to directly increase the per-cell signal propagation distance. Details of these techniques are discussed in Wintzer *et al.*⁴

In 2005, a duality-preserving discrete adjoint approach was introduced for Cart3D.²² This solver shares the same basic data structures, domain decomposition and other infrastructure with the primal solver and achieves similar performance. While originally developed for gradient-based shape optimization,²⁸ the adjoint method was also employed for output error-estimation and adaptive mesh refinement²⁹ using an approach similar to that of others in the literature.^{30–33} This method was first applied directly to boom-propagation

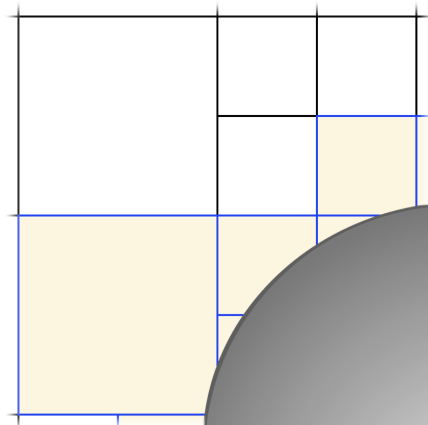


Figure 1. Multilevel Cartesian mesh with a cut-cell boundary.

problems in Ref. [3], where we introduced an off-body field functional written as a pressure sensor in quadratic form.

$$\mathcal{J} = \int_0^L \frac{(p - p_\infty)^2}{p_\infty} dl \quad (2)$$

Integration of this functional is performed along a sensor of length L placed in the field where the signature is measured. With this functional output, the adjoint-based error-estimation then tailors the mesh refinement to reduce the error in the pressure signature at the location of the sensor. Error in this signal can be either driven below some pre-specified value, or alternatively, reduced as much as possible using a worst-errors-first strategy until a desired mesh size is reached. Adaptation is performed incrementally by cycling between the primal and adjoint solvers, with no more than one level of cell refinement being performed at a time. With this strategy, a typical adaptive simulation costs 3-5 times that of a single flow solution on the final mesh.

By convention, a cylindrical coordinate system is used for sonic boom analysis. The longitudinal coordinate x runs axially, and h is the radial coordinate. The azimuthal angle, Φ , measures the angle off-track, and $\Phi = 0^\circ$ is referred to as “on-track”.

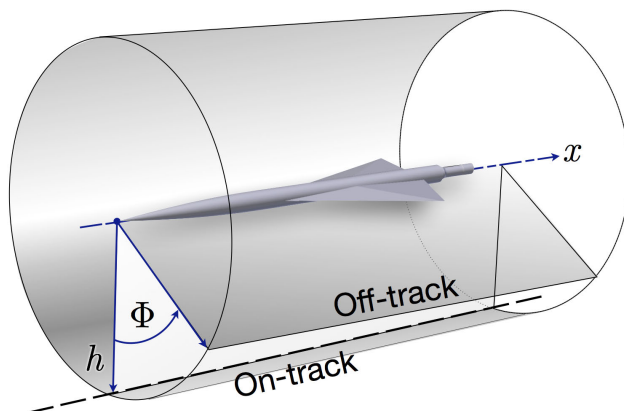


Figure 2. Cylindrical coordinates used for sonic boom.

III. Workshop Results and Investigations

Simulations for the workshop focus on the prediction of near and mid-field pressure signatures for three geometries in supersonic flow. The first two are compulsory while the third is optional. Figure 3 shows a composite image of all three models for reference. The simplest model is a low-boom body of revolution used for instrument and tunnel calibration during testing in 2012 in the NASA Ames 9×7 ft. Supersonic

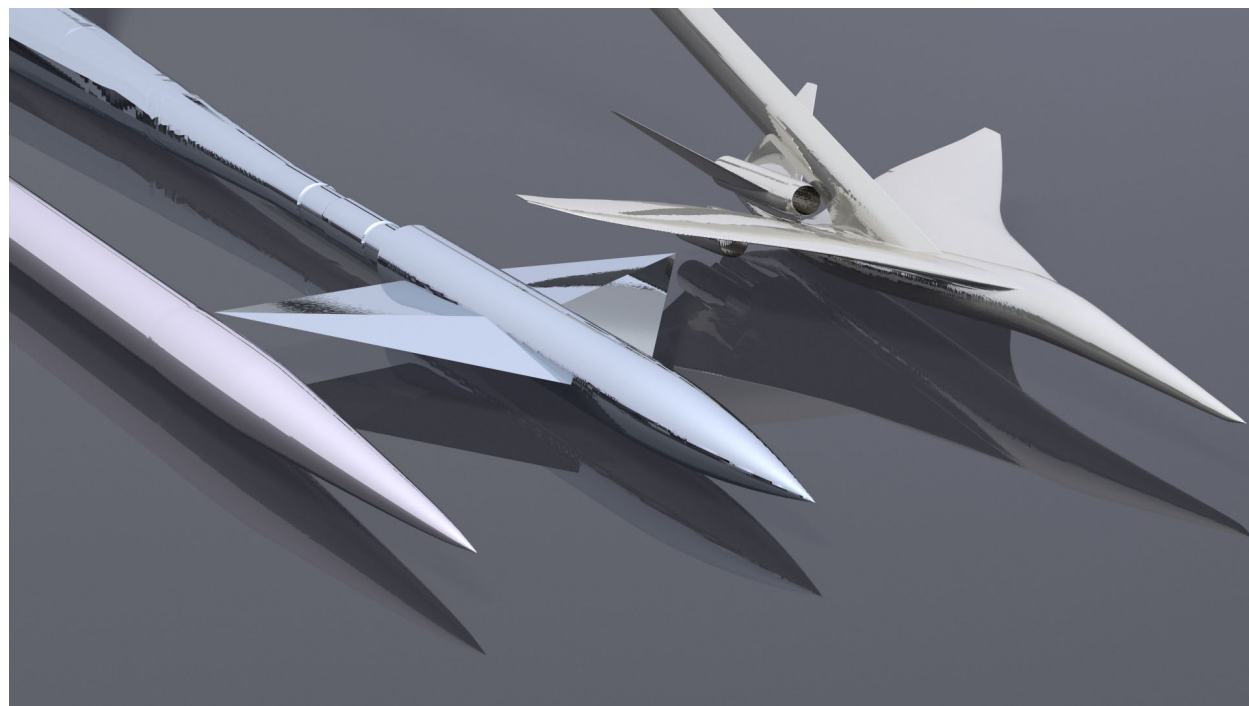


Figure 3. Models for the 1st AIAA Sonic Boom Prediction Workshop. (Left) Axisymmetric Seeb-ALR model. (Center) 69° delta-wing-body. (Right) Lockheed Martin LM1021 Concept. Rendering of discrete geometry. Models not to relative scale.

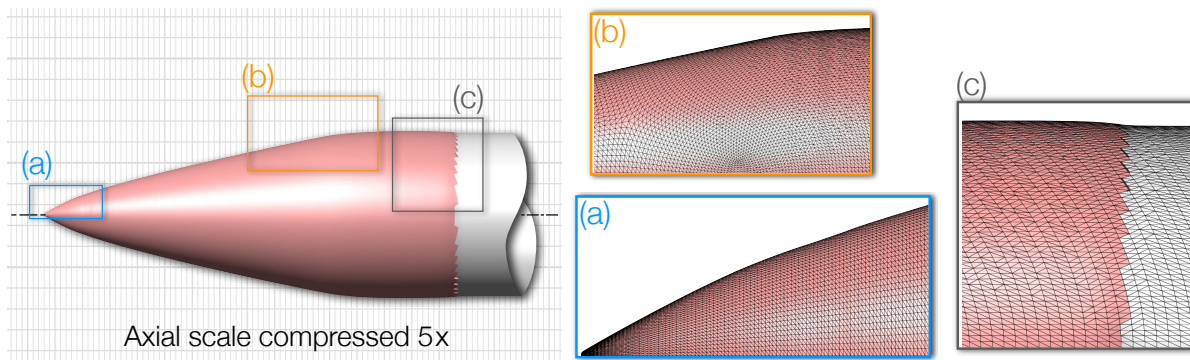
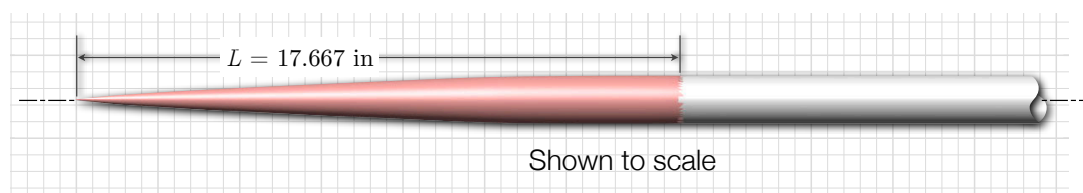


Figure 4. Details of the axisymmetric Seeb-ALR geometry. (Upper) Model shown to scale. (Lower) Model shown with compressed axial scale to highlight regions of curvature. Frames (a), (b), and (c) highlight surface meshing and geometric curvature near the nose, shoulder and rear of the model.

Wind Tunnel. Two winged configurations are also examined. The first is a 69° delta-wing-body shown in the center of Figure 3. This model was originally tested in the same tunnel in 1973,³⁴ and recently re-tested in preparation for the workshop.^{35,36} The final configuration was the most geometrically complex. This was an optional test case examining signature prediction for a complete lifting supersonic transport configuration with flow-through nacelles. This geometry was developed by Lockheed Martin as part of a design study of next-generation configurations for the NASA Fundamental Aeronautics Program's High-Speed Project.^{37,38} The workshop provided both surface triangulations and CAD geometry for all three models. Required submission data included on-track and off-track pressure signatures as well as complete boom-carpets at mid-field locations up to 4.6 body-lengths away from the models.

A. Case 1 – Seeb-ALR

A.1. Seeb-ALR: Geometry

The axisymmetric Seeb-ALR model was constructed by Lockheed Martin and was tested in the NASA Ames 9×7 ft. Supersonic Tunnel in 2012.^{37,38} The model is a body of revolution based upon the work of Darden, George and Seebass.^{39,40} Figure 4 shows various views of this geometry. The “ALR” moniker denotes “Aft Lift Relaxation” which is a design feature that increases the diameter of the geometry slightly to reach a maximum just aft of the shoulder, and then tapers slightly to meet the cylindrical sting extension. Traditional Seeb designs transition monotonically to cylindrical aft-bodies. A reference length of $L=17.667$ in. was specified for the workshop^a and the body reaches its maximum diameter of ~ 1.43 in. around 15.6 in. from the tip. The cylindrical sting has a diameter of 1.395 in. which begins 17.678 in. downstream of the tip. The sting was tapered to a point far downstream in the simulations.

The workshop provided various representations of the Seeb-ALR geometry including surface triangulations, structured surface grids and solid models in both Parasolid and STEP formats. The surface meshes and CAD files represent the “as-built” geometry and were generated by measurement of the actual test article after manufacture.³⁸ The tessellation shown in Figure 4 was generated directly from the Parasolid CAD representation and was crosschecked with the unstructured discrete representation. The final tessellation contains ~ 254 k triangles with good curvature alignment and typical aspect ratios between 2 and 5. Figure 4 shows details of this triangulation near the tip, shoulder and aft cylindrical junction. A scale view of the geometry is shown at the top of this figure with the geometry ahead of the cylindrical portion colored. The

^aThis value is given as 17.678 in. in Ref. [38]

lower frames show the geometry using a compressed axial scale to highlight the change in radius along the axial dimension. Frames (a), (b), and (c) show details of the surface triangulation at the nose, shoulder and aft sections. Close inspection of the nose reveals that while the manufactured model is slope-continuous, the profile has subtle inflection points, and the axial-curvature briefly changes sign about 1.8 in. downstream of the tip. Frame (c) shows details of the cylindrical juncture. Neither solid model had a CAD edge defining this feature. As a result, all the surface triangulations had relatively poor representations of this transition.

A.2. Seeb-ALR: Meshing

Figure 5 shows symmetry plane views of the computational mesh and computed isobars from the final simulation. Following the methods outlined in Refs. [3] & [4], the mesh was rotated to roughly the Mach angle of the free stream flow, and the cells were stretched roughly 2:1 along the dominant direction of wave propagation. This figure also shows the locations of pressure sensors at $h = 21.2$ in. and $h = 42.0$ in. directly on-track ($\Phi = 0^\circ$). The objective of this case was to obtain accurate off-body signatures at the sensors. Therefore, the adaptation was driven using a simple functional comprised of the weighted sum of the pressure signals on the two sensors following eq. (2), with the signal at 42 in. receiving four times the weight of that at 21.2 in. to account for the weaker signal at this distance. The starting mesh is shown on the left (~ 25 k cells) and had a region of nearly uniform refinement covering both the geometry and sensor locations. After 7 cycles of adaptive refinement, the cell count grew to 2.01 M cells as shown in the middle image of Figure 5. The computed pressure signals along these sensors on the mesh shown were submitted to the workshop. On the right, isobars in the discrete solution give a sense of the evolution of the pressure signal between the body and the sensors. The color map is chosen so that white indicates free stream and red and blue indicate higher and lower relative pressures. This shading makes apparent the quick change from over-pressure to expansion emanating from the shoulder region of the geometry (see detail in frame (b) of Figure 4). Note that the small glitch downstream of the Seeb-ALR geometry (faintly visible in the isobars) is simply an artifact of the sting extension which happens to get picked up by the sensors and is downstream of the region of interest.

A.3. Seeb-ALR: Mesh Convergence

While workshop results were submitted from the discrete solution after 7 cycles of adaptive refinement, two additional refinements were performed to verify and quantify the degree of mesh convergence. Figures 6 & 7 present this evidence from three perspectives: convergence of the functional, convergence of the adjoint-based error estimates and evolution of the pressure signal at the sensors. The frame at the left of Figure 6

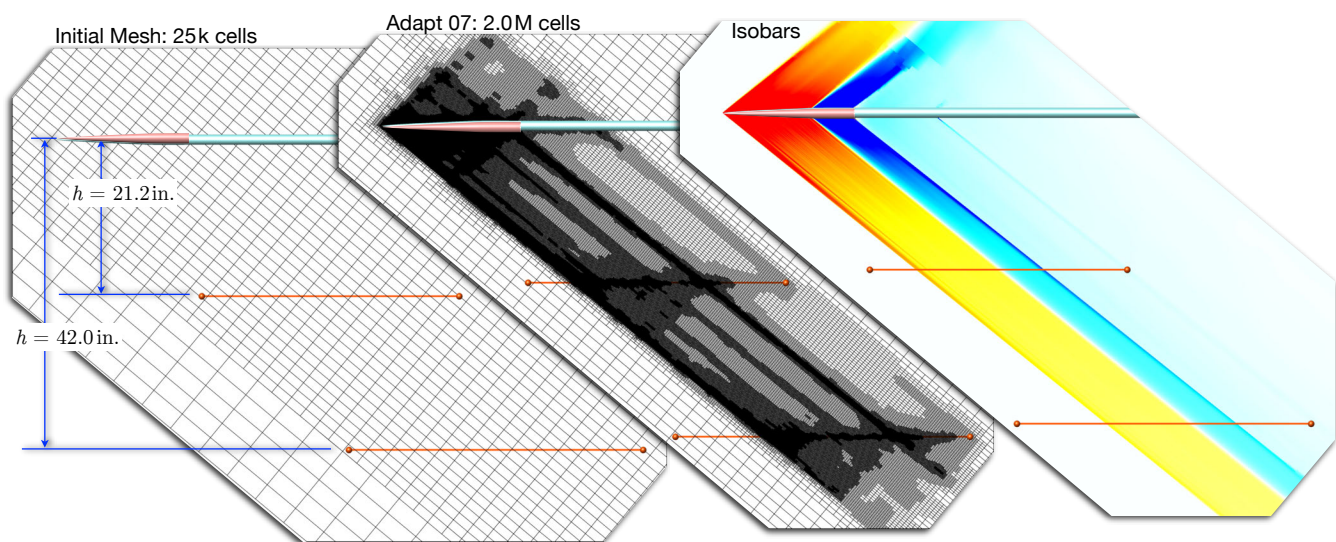


Figure 5. Symmetry plane mesh and isobars in discrete solution for Mach 1.6 flow over the “as-built” Seeb-ALR geometry at $\alpha = 0^\circ$. Initial mesh contains ~ 25 k cells. Mesh after 7 cycles of adaptive refinement contains 2.01 M cells.

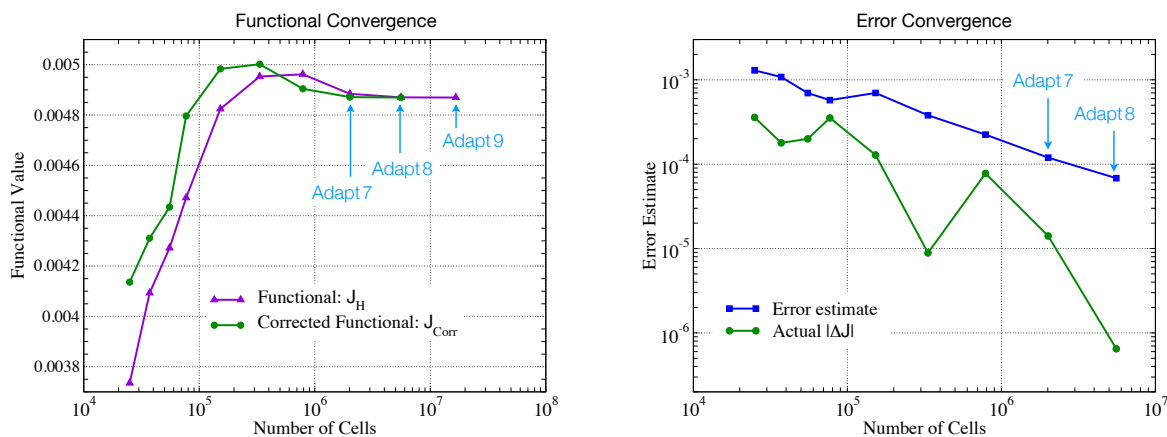


Figure 6. Mesh convergence for Seeb-ALR case. (Left) Convergence of the functional and adjoint correction. (Right) Convergence of the adjoint-based error estimate and actual update to the functional, $|\Delta \mathcal{J}|$.

shows convergence of the output functional, \mathcal{J} . Mesh convergence is achieved when this objective stops changing with further refinement. The abscissa of this plot gives the number of cells and the symbols on the curves correspond to adaptation cycles. Cycles 7, 8 and 9 are labeled. Since the functional is an integral of pressure along the sensors, this plot shows that the simulation values along the extraction lines are becoming increasingly independent of the mesh as we refine. On each mesh, the adjoint solution also provides a correction to the functional based on a linearization about the current discrete solution.³ The corrected functional is shown in green (circles) on this plot. As expected, the corrected functional *leads* the computed objective by approximately one adaptation cycle, and the correction itself vanishes rapidly as the mesh is refined.

At the right, Figure 6 shows error convergence as the mesh is adaptively refined. The plot tracks convergence of both the estimate of the error-bound on \mathcal{J} computed from the adjoint solution as well as the actual change in the magnitude of the functional $|\Delta \mathcal{J}_n| \equiv |\mathcal{J}_n - \mathcal{J}_{n+1}|$ observed after each cycle of adaptive refinement. In the Richardson region, the adjoint-based error estimate (blue) should decrease linearly on a *log-log* plot. We observe this textbook behavior over the last five adaptation cycles. Despite the strong non-linearities in the flow, the solution appears to be converging asymptotically giving a high degree of confidence in the discrete solution on the final few meshes. Further confirmation is provided by the behavior of $|\Delta \mathcal{J}|$, which is everywhere below the estimated error-bound, indicating that the update is well behaved, and the bound is conservative. After 8 cycles of refinement the error-bound corresponds to about the height of one symbol on the plot of functional convergence. The final update going from 8 to 9 ($|\Delta \mathcal{J}_8|$) is about two orders of magnitude smaller still. In production mode, the adaptation module does not solve the adjoint on the finest mesh, so the final error estimate is for the “Adapt 8” mesh.

Figure 7 shows evolution of pressure signal at $h = 21.2$ in. and $h = 42.0$ in. over the final few adaptation cycles. These both show that the solution is essentially unchanging – as expected from the convergence of the functional and error estimates already presented. While we do observe some sharpening of the highest

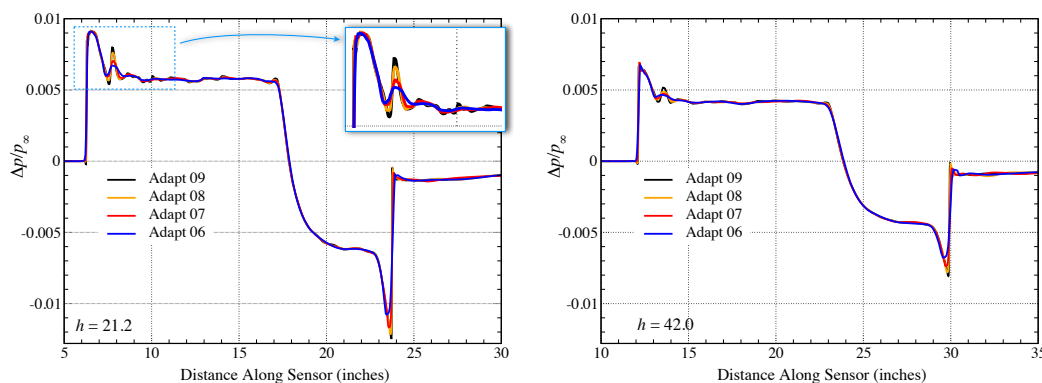


Figure 7. Convergence of the off-body pressure signature with mesh refinement for Seeb-ALR at $h = 21.2$ in. (left) and $h = 42.0$ in. (right).

Tunnel Runs	Reference Run	M_∞	α	β	Altitude, h
553-578	#580	1.6	-0.27°	0.17°	20.62 in.
195-219	#221	1.6	-0.29°	0.17°	20.59 in.

Table 1. Nominal tunnel conditions, run numbers and reference signatures used in Seeb-ALR comparison at $h = 21.2$ in.

frequencies in the pressure profiles, the overall levels of the main compression and expansions are essentially constant from adapt cycles 6 (789k cells) through 9 (16.6M cells). Note in particular that the strength of the initial peak, the pressure through the flat-top region, and the profile of the main expansion do not differ substantially despite a 20-fold increase in cell count over the range of these solutions.

A.4. Seeb-ALR: Data Comparisons

Figures 8 and 9 show comparisons of the mesh-converged pressure signatures with both predictions based on linear theory and experimental measurement. Experimental data are only available for the signature at $h = 21.2$ in. and both figures focus on this location. In Ref. [38], Figure 18 showed the pressure profile at this location as predicted by a simulation using an in-house analysis tool based on linear theory. That simulation used the same CAD geometry as was used in our current study. Figure 8 overplots the results from that analysis with the mesh converged pressure signature from our inviscid simulations. Agreement between Lockheed's linear analysis and our inviscid Cartesian method is remarkably good. Not only do the flat-top overpressure (near $2 \leq x \leq 10$) and main expansions (near $11 \leq x \leq 17$) agree both in shape and magnitude, but much of the high frequency content is also well represented. The slight discrepancy in the magnitude of the initial shock is most likely a shortcoming of the linear theory where the geometry's slightly blunted nose creates a small detached bow-shock accompanied by non-linear flow physics in this Mach 1.6 free stream. The second peak near the front of the signal stems from the inflection point on the geometry noted at the end of §III.A.1 and shown in detail in Figure 4(a).

Figure 9 presents a comparison of the computed pressure signature with the most relevant tunnel data available. Reference run signatures #580 and #221 correspond to run series 553-578 and 195-219 respectively.^{38,41} Measured data for each set of runs were processed using the spatial and temporal averaging method from Refs. [35] and [36] to produce the mean and standard deviation data for each reference signature. Table 1 gives nominal conditions for these two composite signatures. In both cases, $M_\infty = 1.6$ and the angle of attack was slightly negative, $\alpha \approx -0.3^\circ$ and the signatures were measured at a height of around 20.6 in. Data showing these two reference signatures are shown in red and orange in Figure 9. The grey envelope indicates the 1σ standard deviation of the aggregated signatures.

Comparison of the adaptive simulations with the experimental measurement is excellent through the initial compression and the major high-frequency peaks settling into the flat-top pressure along the forebody.

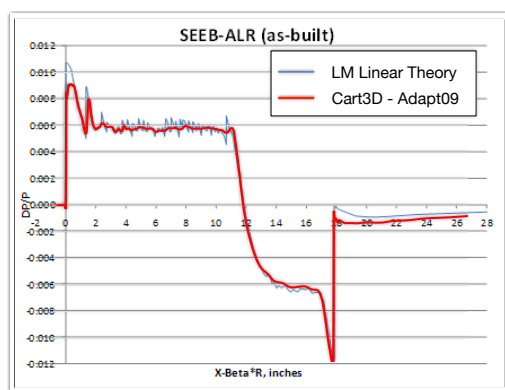


Figure 8. Overplot of pressure signature at $h = 21.2$ in. with predictions from linear theory (reprinted from Ref. [38], Fig.18.) using the same CAD descriptions of the geometry. $M_\infty = 1.6$, $\alpha = 0^\circ$.

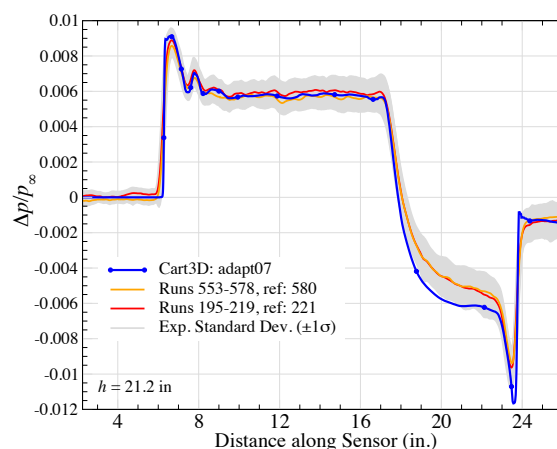


Figure 9. Comparison with tunnel measurements. Tunnel data used spatial and temporal averaging. 1σ standard deviation of measurements shown.³⁵ Data from Ref. [41]. $M_\infty = 1.6$, $\alpha = 0^\circ$.

Some discrepancy is present through the main expansion where the simulation falls near the lower edge of the 1σ envelope. This feature emanates from the curvature of the shoulder of the geometry shown in Figure 4b. In this region, the inviscid simulations agree closely with not only Lockheed's linear method, but also with published calculations done with Navier-Stokes (laminar and turbulent) methods.^{36,38,41} Given the degree of mesh convergence, and the consistency of the simulation results across this spectrum of physical models, we undertook a detailed comparison of the CAD model with the actual Seeb-ALR test article. Hand measurements using a digital caliper and a makeshift jig confirmed the model's fidelity to within measurement accuracy (± 0.002 in).^b

A more likely source of this discrepancy is interaction with the pressure rail. Ref. [35] shows simulations of the Seeb-ALR model with the pressure rail mounted in the tunnel. When the model was positioned toward the front of the rail, the predicted signatures show a distortion of the main expansion due to interaction with the rail very similar to the discrepancy seen in Figure 9 (see Fig. 10 in Ref. [35]). The model position and h/L in that analysis was within a few inches of this case, and the predicted distortion in the expansion is very similar. Note that Ref. [38] reports similar behavior in simulations of the "OptSig" model which was tested along with the Seeb-ALR and also mounted near the front of the pressure rail.

Simulation results on the 2.01 M cell mesh shown in Figure 5 were submitted to the workshop. This case was run on a 2011-era laptop with four Xeon i7 cores. The total memory used was under 3.6 GB. Total wall-clock time including initial mesh generation, all adaptation cycles and flow and adjoint solution time was about 1 hour (61 min.) using all four hardware cores.

B. Case 2 – 69° Delta-Wing-Body (DWB)

Originally identified as "Model 4" in the 1973 wind tunnel study by Hunton and Hicks *et al.*,³⁴ the delta-wing-body shown in Figure 10 is the simplest winged configuration considered in the workshop. The figure shows perspective renderings as well as planform, side and sectional views of this geometry. The model is an analytically defined tangent-ogive-cylinder on a sharp delta-wing with a 5% thick diamond cross section. This geometry has been the subject of numerous numerical studies^{4,42,43} and was also one of the configurations studied by the NASA Fundamental Aeronautics workshop in 2008.²⁰ Simulations for the present workshop were conducted at $M_\infty = 1.7$ and $\alpha = 0^\circ$.

B.1. DWB: Geometry

In October 2012, the DWB model was fitted with a new sting and re-tested in the NASA Ames 9×7 ft. Supersonic Wind Tunnel using a newly developed pressure rail for signature measurement.^{c,35} Figure 10 shows the front portion of the new sting and its attachment at the model's base. At NASA's earlier workshop

^bRef. [38] gives the claimed accuracy of the the CAD description as ~ 0.0003 in.

^cThis test was entry T97-0251 in the Ames Unitary Plan facility, Oct. 2012.

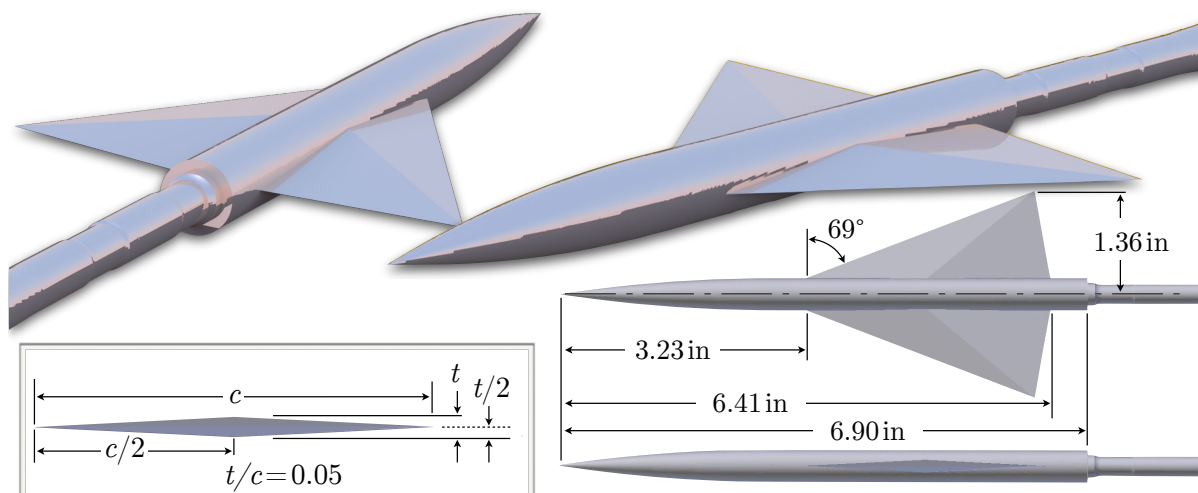


Figure 10. Planform, side and perspective renderings of the delta-wing-body from NASA TN-D 7160³⁴ used for workshop case 2. The model is shown with the sting fitted for the Ames 9×7 ft. Unitary Plan Supersonic Tunnel tests in 2012.

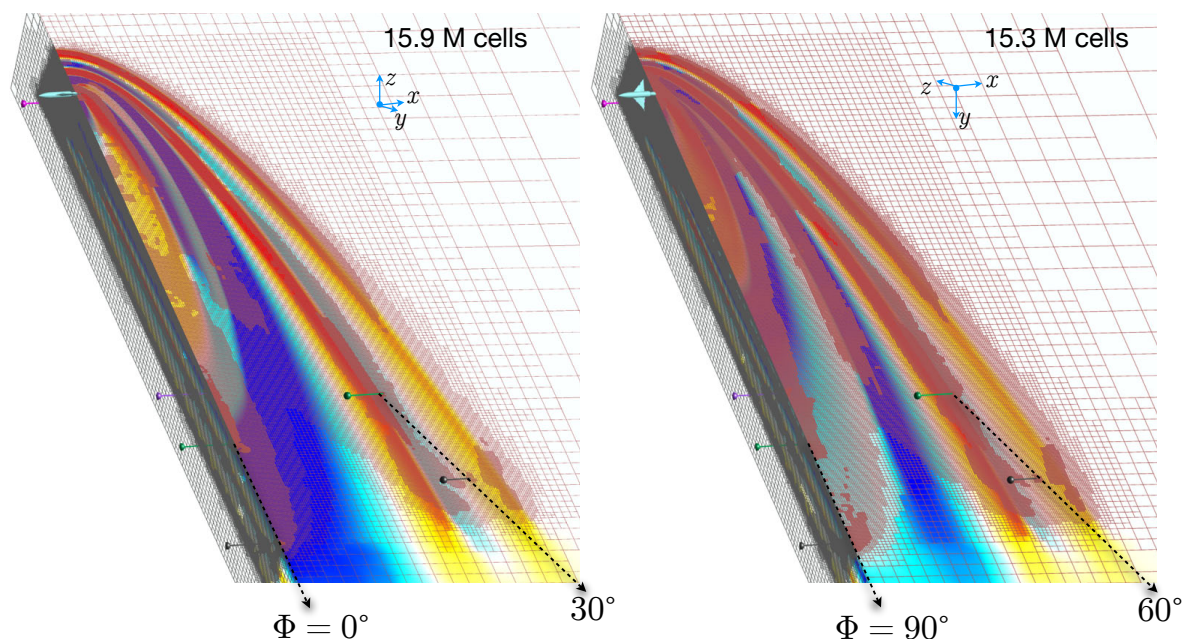


Figure 11. Case 2: Adapted Cartesian mesh and solution isobars for 69° delta-wing-body at $M_\infty = 1.7$ and $\alpha = 0^\circ$. Pressures were extracted at off-body distances of $h = \{0.5, 21.2, 24.8, 31.8\}$ in. (Left) Mesh for $\Phi = \{0^\circ, 30^\circ\}$, with 15.9 M cells. (Right) Mesh for $\Phi = \{60^\circ, 90^\circ\}$, with 15.3 M cells.

in 2008, the geometries used by various simulation codes differed in their treatment of the sting and base leading to slight differences in the results at particular h/L distances for certain lift coefficients.²⁰ By providing a unified description of the geometry, the current workshop directly addresses this ambiguity.

From nose to base, the fuselage of the model measures 6.90 in. long. The delta wing reaches a maximum span of 2.72 in. and the leading edge is swept 69° with a 5% thick diamond cross section as shown in the inset of Figure 10. The workshop provided the model and sting geometry through structured and unstructured surface meshes as well as solid models in both Parasolid and STEP formats. The surface triangulations were derived from the discrete models provided,^d however the model was reflected about the symmetry plane, and the sting was extended about 5 body lengths downstream. In all, the triangulation had ~226 k triangles with reasonably good curvature alignment, except at the very tip of the nose.

B.2. DWB: Meshing

The wind tunnel measurements were conducted at various heights and roll angles to obtain on-track and off-track signatures up to 90°. The workshop called for pressure signatures at $h = \{0.5, 21.2, 24.8, 31.8\}$ inches. When normalized by the body length, these correspond to $h/L = \{0.07, 3.07, 3.60, 4.61\}$, respectively. On track signatures were required at 0.5 in. and 21.2 in. and off-track data was requested at 24.8 in. and 31.8 in. for azimuths of $\Phi = \{0^\circ, 30^\circ, 60^\circ, 90^\circ\}$. Given that these off-track extractions correspond to non-dimensional heights of up to $h/L = 4.6$, obtaining accurate pressures at relatively large distances suggests substantially higher meshing requirements than the Seeb-ALR example.

While the mesh rotation and stretching used in §III.A on the axisymmetric body is representative of the approach used for practical boom calculations, these meshing techniques are clearly designed to promote wave propagation along dominant characteristics of the flow. In a 2011 study,⁴⁴ we quantified the off-track meshing requirements on rotated and stretched meshes and found that achieving comparable accuracy at an azimuth of $\Phi = 45^\circ$ required ~30% more resolution than on-track sensors at the same distance with cosine-like variation in between. For practical boom calculations, the maximum relevant azimuth is limited by the signal cut-off angle of the atmosphere, which is typically between 30° and 50°. Nevertheless, the 2011 study does suggest that it is more cost effective to run the extreme workshop azimuths with the mesh rotated in yaw rather than in pitch. This approach mimics what is done experimentally – where the model roll is used to obtain data at various azimuths. Ultimately, two simulations were performed, one with the mesh rotated and stretched in the pitch-plane (for $\Phi = 0^\circ, 30^\circ$) and one with the mesh yawed (for $\Phi = 60^\circ, 90^\circ$).

Figure 11 shows three-quarter views of the final adaptively refined meshes for simulations at $M_\infty = 1.7$

^dFile “delta_sting_split_s100.tri” provided on the workshop ftp server <ftp://lbpw-ftp.larc.nasa.gov>.

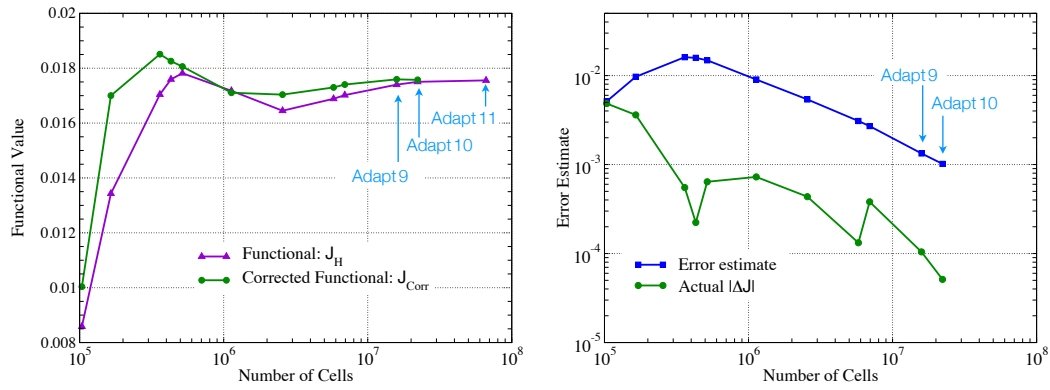


Figure 12. Mesh convergence for 69° DWB case. (Left) Convergence of the functional and adjoint correction. (Right) Convergence of the adjoint-based error estimate and actual update to the functional, $|\Delta J|$.

and $\alpha = 0^\circ$ with locations of the pressure sensors identified. Mesh adaptation was driven by a composite functional comprised of the weighted sum of the pressure signals on each sensor following eq. (2). Contributions from each sensor were weighted by h/L , and off-track sensors were weighted $2\times$ greater than their on-track counterparts. In both cases, the initial mesh size started at ~ 103 k cells and grew to ~ 15 M cells after 9 cycles of adjoint-driven adaptive refinement. The figure includes symmetry plane and crossflow cuts through the mesh, with the location of sensors identified. Mesh adaptation in Figure 11 generally tracks the main pressure disturbances along conic-sections that propagate toward the off-body sensors.

B.3. DWB: Mesh Convergence

Workshop results for the 69° delta-wing-body were submitted for the meshes shown in Figure 11 with 15 M cells after 9 cycles of adaptive refinement. As with the Seeb-ALR case, two additional refinements were performed to establish mesh convergence. Figure 12 shows results for convergence of the adaptation functional (left) and convergence of the adjoint-based error estimates (right). Adaptation cycles 9, 10 & 11 are labeled. As before, the functional is an integral of pressure along the sensors, and this plot shows that the pressure signatures are becoming mesh independent with increasing resolution. The corrected functional (green circles) again leads the computed functional by approximately one mesh, and vanishes rapidly as the mesh is refined. The frame at the right of Figure 12 shows that the estimated error-bound is also well-behaved and is everywhere conservative when compared with the actual $|\Delta J|$. As before, convergence is essentially linear on this *log-log* plot despite the strong non-linearities in this Mach 1.7 flow. This smooth error convergence provides a high degree of confidence in the extracted pressure signals.

Figure 13 presents further evidence of mesh convergence through direct comparison of the evolving pressure signal on-track ($\Phi = 0^\circ$) at $h = 0.5$ in. and $h = 21.2$ in. over the final four adaptation cycles. Mesh convergence at these locations is worth examining since experimental data does not exist in these neighborhoods at comparable conditions.^e Even the coarsest result shows good convergence and only the high frequency features near the aft portion of the signal distinguish the finer meshes. The frame at the right of Figure 13 shows mesh convergence of the off-track signature at $h = 24.8$ in., $\Phi = 60^\circ$.

^eThe closest data at $h = 21.2$ in. is at $\alpha = 0.7^\circ$ and no data was taken at $h = 0.5$ in.⁴¹

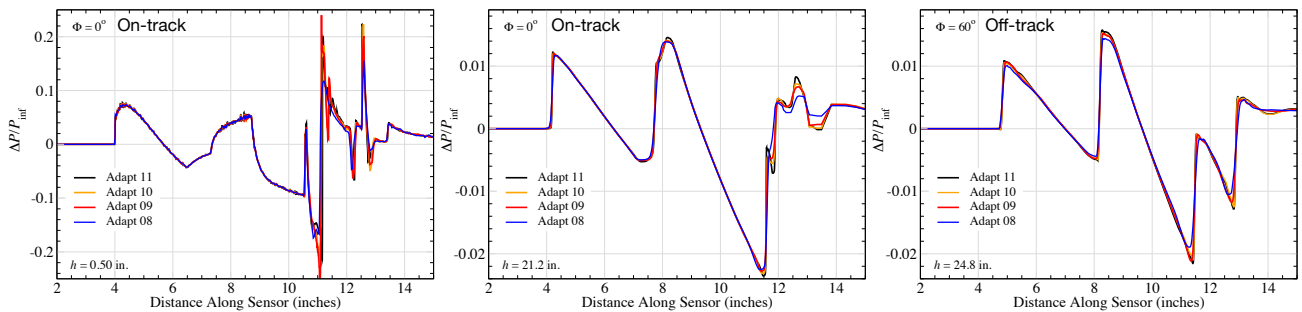


Figure 13. Convergence of the off-body pressure signature with mesh refinement for 69° delta-wing-body case near the body at (left) $h = 0.50$ in., $\Phi = 0^\circ$, (center) in the mid-field $h = 21.2$ in., $\Phi = 0^\circ$, (right) mid-field, off-track $h = 24.8$ in., $\Phi = 60^\circ$.

Tunnel Runs	Reference Run	M_∞	α	Φ	Altitude, h
5598-5637	#5638	1.7	0.24	0.16°	24.86 in.
5530-5549	#5550	1.7	-0.20	29.97°	24.75 in.
5551-5570	#5571	1.7	-0.18	60.06°	24.75 in.
5572-5591	#5592	1.7	-0.18	89.87°	24.69 in.
5240-5274	#5275	1.7	-0.06	0.60°	31.64 in.
5284-5301	#5275	1.7	-0.17	29.94°	31.74 in.
5310-5327	#5328	1.7	-0.22	59.74°	31.56 in.
5336-5354	#5354	1.7	-0.20	89.96°	31.61 in.

Table 2. Nominal tunnel conditions, run numbers and reference signatures used for 69° DWB pressure signature at $h = 24.8$ & 31.8 in.

B.4. DWB: Data Comparisons

While relevant experimental data was unavailable for the two signals at 0.5 & 21.2 in., on-condition data was recently published at both $h = 24.8$ in. and $h = 31.8$ in. for the full range of all azimuths considered in the workshop, $\Phi = \{0^\circ, 30^\circ, 60^\circ, 90^\circ\}$.^{41,45} Table 2 details the nominal tunnel conditions, run numbers and reference signatures used for the experimental data. In all cases, the angles are within 0.25° and the pressure rail was within 0.25 in. of the sensor locations used in the simulations. Figures 14 and 15 show direct comparison of the pressure signatures at $h = 24.8$ in. and $h = 31.8$ in. with the experimental data. Since these plots maintain consistent axes, comparing at the two heights gives a sense of the weakening of the signal as it propagates away from the body.

Agreement between simulation and experiment is good across all locations, and comparisons with the RANS results found in Refs. [41] and [45] are excellent – even at the most extreme azimuths. As the signal moves off-track from the centerline, there is an interesting trend seen in both the experiment and simulation. On-track, the simulation catches a very tight expansion mid-way up the final re-compression (see Fig. 14: $\Phi = 0^\circ$, ~ 11.8 in.). RANS simulations with NASA's OVERFLOW solver showed the same feature,⁴⁵ and it first becomes noticeable in the experimental data at $\Phi = 30^\circ$. As the azimuth angle increases, this feature lengthens substantially until it dominates the re-compression at $\Phi = 60^\circ$ and 90° .

As with the Seeb data presented earlier, the experimental data is a composite obtained using spatial and temporal averaging of the data along the pressure rail and then removing the background signal of the tunnel (the “reference signature”). References [35,36,41] and [45] discuss the development and application of the measurement techniques used to obtain the experimental pressure signatures. These authors note the many challenges associated with accurately measuring the weak disturbances from small models in large supersonic tunnels. Extracting clean experimental data from this low signal-to-noise environment requires substantial post-processing. Some evidence of the degree of measurement scatter is shown by the grey shaded regions in the pressure signature plots which show the 1σ standard deviation of the experimental data over the averaging window. In the eight comparison plots shown in Figures 14 and 15, the simulation data consistently matches the experiment very well. However, inspection of any one of these reveals that the simulation data exhibits peaks that are both higher and sharper than the corresponding measurements. These same characteristics were shown for simulations with NASA's USM3D code in Refs. [41] and [45]. Additionally, the experimental data consistently shows compressions that are decidedly less steep than the crisp shocks found in the CFD signatures. In their development of the measurement techniques, Morgenstern, Cliff and Durson cite numerous reasons for the rounding and relaxing of the experimental data.^{35,36,41,45} Most notably, tunnel turbulence and other unsteadiness contribute to high frequency model vibration which smoothes the pressure profile, aggressively eroding sharp peaks. These effects become more pronounced as the propagation distance increases. Other leading contributors are humidity in the tunnel, the location of the model with respect to the rail and the post-processing techniques themselves. In Ref. [36] Morgenstern states bluntly *A high resolution CFD solution should be more “peaked” than wind tunnel measurements and [would] require similar displacement vibration rounding for spikes to match measurements.* Cliff noted that the degree of rounding of the experimental signatures due to model vibration increased with h/L .^{41,45} On this small model, the 24.8 in. and 31.8 in. heights correspond to normalized propagation distances of 3.6 and 4.6 body lengths. These are 3 to 4 times larger than the $h/L = 1.2$ of the Seeb-ALR signature in Figure 9, which could result in significantly more rounding of the data.

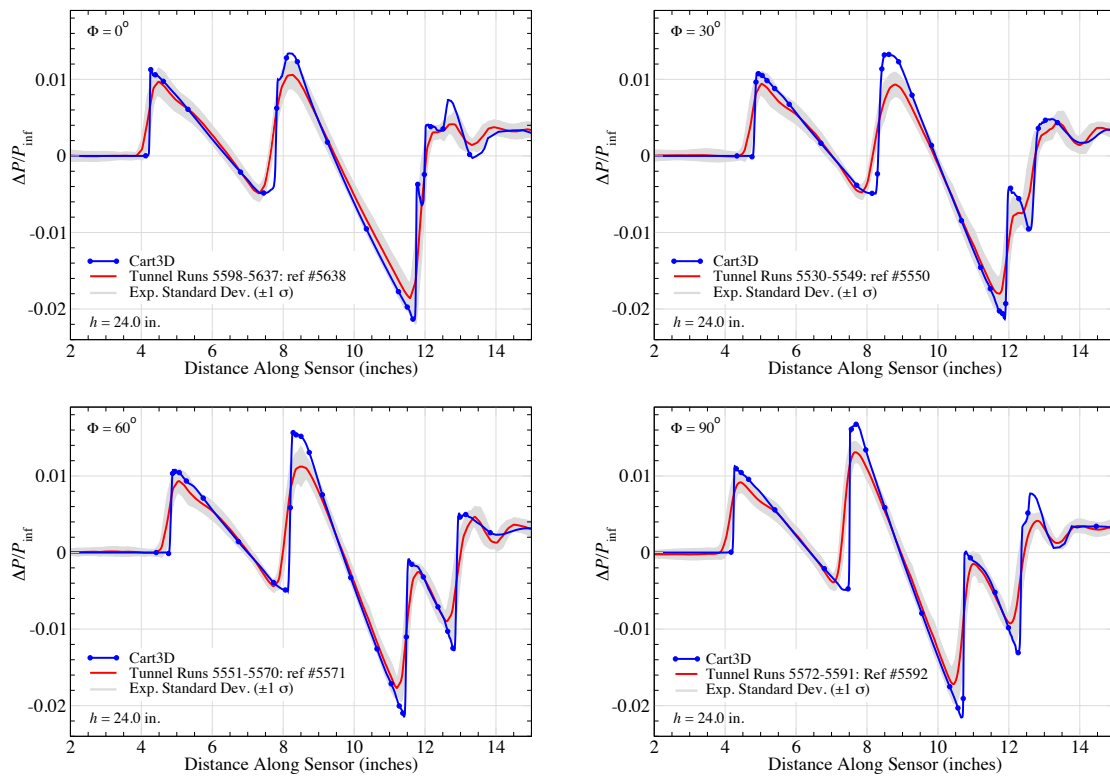


Figure 14. On-track and off-track comparison of pressure signatures with tunnel measurements at $h = 24.8$ in for azimuths $\Phi = \{0^\circ, 30^\circ, 60^\circ, 90^\circ\}$. Tunnel data used spatial and temporal averaging. 1σ standard deviation of measurements shown.³⁵ Data from Ref. [41]. $M_\infty = 1.7$, $\alpha = 0^\circ$.

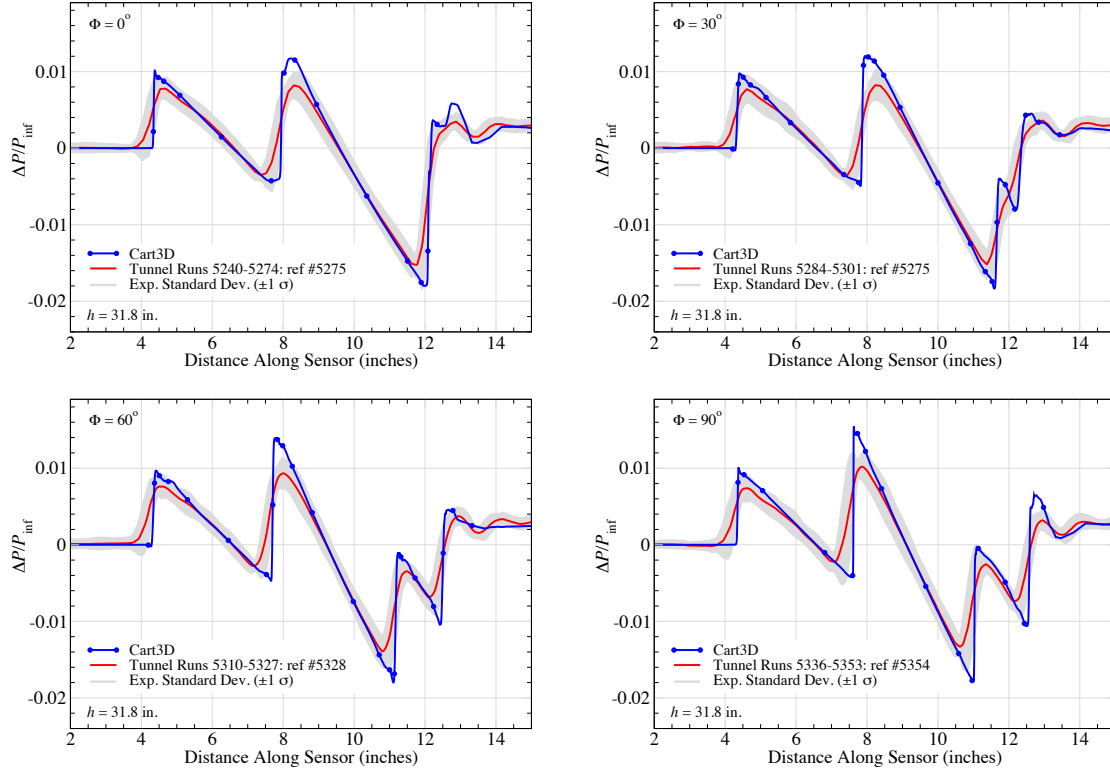


Figure 15. On-track and off-track comparison of pressure signatures with tunnel measurements at $h = 31.8$ in for azimuths $\Phi = \{0^\circ, 30^\circ, 60^\circ, 90^\circ\}$. Tunnel data used spatial and temporal averaging. 1σ standard deviation of measurements shown.³⁵ Data from Ref. [41]. $M_\infty = 1.7$, $\alpha = 0^\circ$.

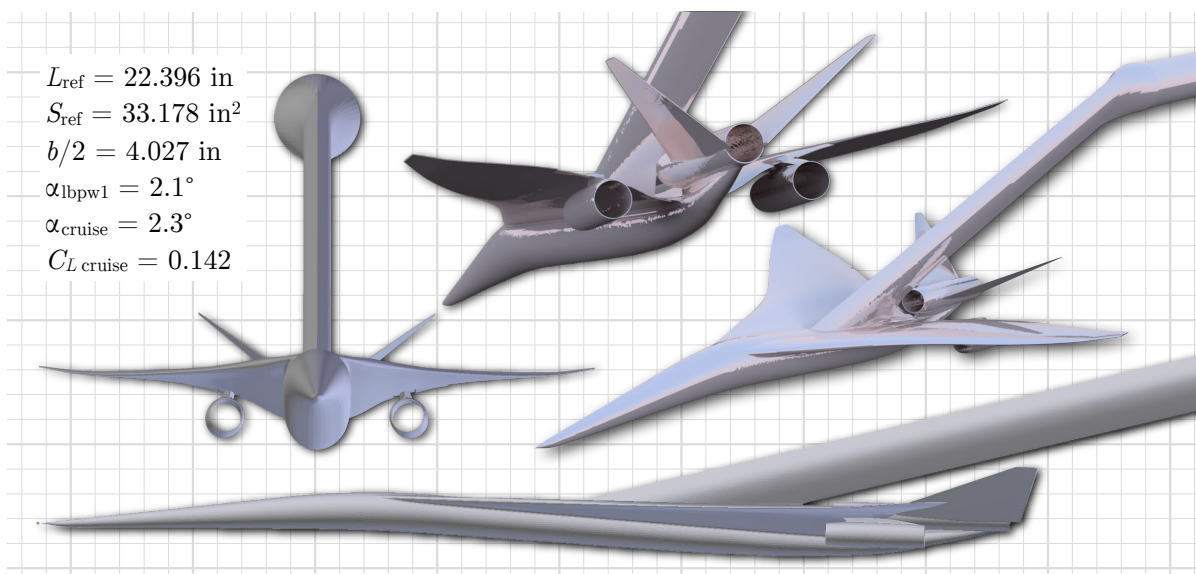


Figure 16. Front, side and three-quarter views of the Lockheed Martin model 1021 tri-jet geometry with blade-sting as tested in the NASA Ames 9×7 ft. Supersonic Tunnel. Workshop cases were at $M_\infty = 1.6$, $\alpha = 2.1^\circ$

Simulation results on the meshes shown in Figures 11 were submitted to the workshop. This case was run on a dual-socket system with a 20 hardware cores.^f Each simulation used under 36 GB of total memory, and the total wall-clock time including initial mesh generation, adaptation, flow and adjoint solution time was just under one hour.

C. Case 3 – Lockheed Martin 1021 Model (LM 1021)

The final case considered in the workshop was an optional study of a complete aircraft configuration designed for low sonic boom. This configuration was designed by Lockheed Martin Corp. and was tested jointly with NASA in the same tunnel as the previous two cases. The LM 1021 design was developed during Phase I of Fundamental Aeronautics' study of next generation low-boom designs.³⁷ Figure 16 shows an overview of the configuration through front, side and three-quarter views of the complete geometry. To permit accurate signature measurement, the model used a blade-sting attached atop the fuselage for mounting in the tunnel. Wind tunnel testing was conducted in October 2011, April 2012 and October 2012. The workshop simulations were all computed at Mach 1.6 and 2.1° angle of attack.

C.1. LM1021: Geometry

The table inset in Figure 16 gives key reference quantities for the 1/125th (0.8%) scale tunnel model. With a reference length of 22.4 in., LM1021 is almost four times larger than the 69° delta wing model studied in the previous section. Despite the model's overall size, the V-tail, flaps and three flow-through nacelles introduce extremely fine scales, and many of the features near the aft-end had to be manufactured thicker on the tunnel model than in the full-scale design.

The workshop provided the model and sting geometry in both STEP and IGES formats. Additionally, watertight surface triangulations of the half-body were provided in both CGNS and Cart3D formats. The surface triangulations rendered in Figure 16 were derived from these discrete models,^g however the model was mirrored about the symmetry plane and the sting was extended about 2.5 body lengths downstream. In total, the surface triangulation had 398 k triangles. This tessellation had relatively poor curvature alignment along the wing leading edges, the wing-body juncture, on the nacelles and near the nose; some artifacts of this poor alignment are visible in Figure 16.

^f2× Intel Xeon E5-2680v2, with 10 cores each.

^gFile "LM_1021mody.tri" provided on the workshop ftp server <ftp://lbpw-ftp.larc.nasa.gov>.

C.2. LM1021: Meshing

The tunnel measurements were taken at heights varying from 20 to 70 in. and roll angles from 0° to 48° to obtain on and off-track signatures.⁴⁵ Surveys up to $h = 42$ in. were conducted with the rail mounted in the forward position of the test section which generally provides better data quality.^{36,41} The workshop requested pressure signatures at $h = \{1.64, 2.65, 3.50, 5.83, 8.39\}$ ft. When normalized by the reference length, these correspond to distances of $h/L = \{0.88, 1.42, 1.88, 3.13, 4.50\}$. Complete signature carpets were requested for each h/L covering the entire range from directly under the model ($\Phi = 0^\circ$) to directly overhead ($\Phi = 180^\circ$). We constructed these carpets using an array of pressure sensors at each h/L with azimuthal spacing of 10° . These sensor arrays started at $\Phi = 0^\circ$ and extended to a maximum off-track angle of 50° .^h This array of 30 sensors was sufficient to provide pressure carpets from on-track to signal cutoff at each of the five h/L 's and encompassed the full range of experimental data. Accurately propagating signals from this highly detailed configuration over long distances for a broad range of azimuth angles portends substantially higher meshing requirements than in either of the preceding examples.

As in the earlier examples, the squared-form of the pressure sensors in eq.(2) was used to drive mesh adaptation. Contributions from each sensor were weighted for both h/L and azimuth angle to account for the signals weakening with propagation distance and off-track meshing efficiency. The net functional was a combination of the weighted contributions from the M sensors in the array:

$$\mathcal{J} = \sum_{i=1}^M w_i \mathcal{J}_i \quad \text{with} \quad w_i = \frac{h_i}{L_{\text{ref}}} \left(1 + \frac{4}{\sqrt{2}} \sin \Phi_i\right) \quad (3)$$

These weights were developed empirically with a goal of roughly equilibrating the contributions from each sensor to the net functional. Also note that the scheme in eq.(3) yields similar weights as those described for the 69° DWB case presented earlier, and has been used in numerous internal investigations – including simulations of the full-scale LM1021 configuration.

Figures 17 and 18 present symmetry plane and three-quarter views of both the sensor array and the adapted Cartesian mesh. Sensors are colored by h/L and the mesh is highlighted by local pressure to show

^hNo attempt was made to extend these carpets above the horizon since such data is irrelevant for boom signatures and would be dominated by the mounting hardware in this particular case.

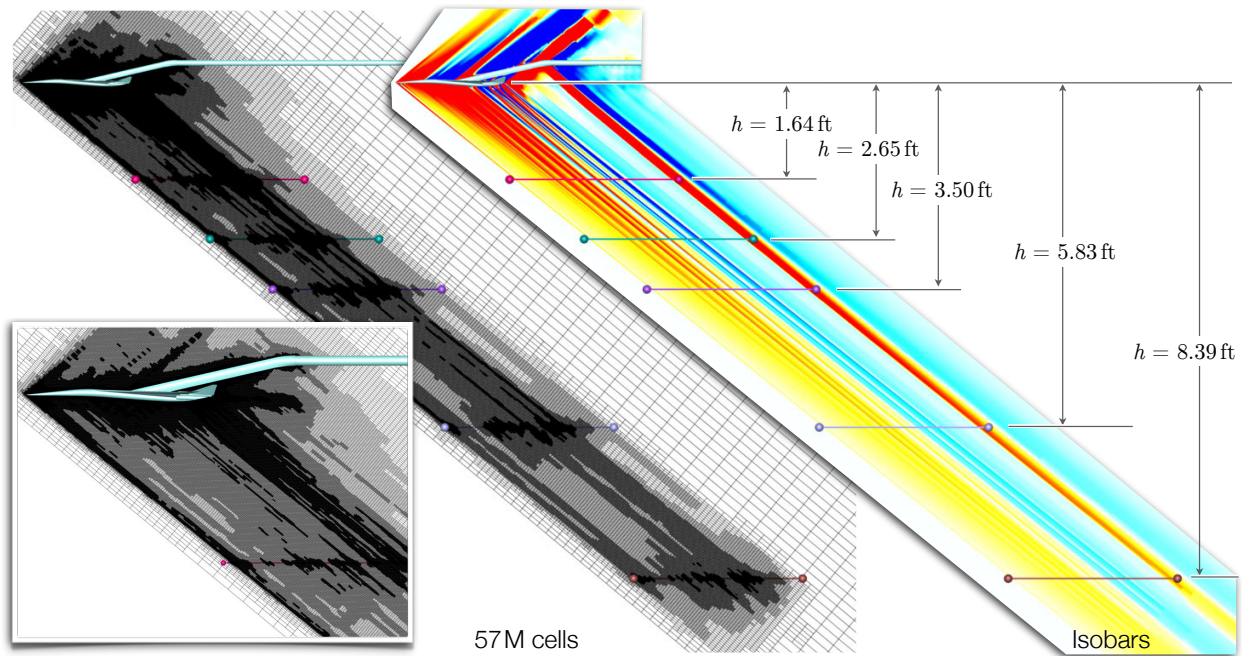


Figure 17. Case 3: Symmetry plane Cartesian mesh and isobars for Lockheed Martin tri-jet LM1021 at $M_\infty = 1.6$, $\alpha = 2.1^\circ$. Pressures were extracted at off-body distances of $h = \{1.64, 2.65, 3.50, 5.83, 8.39\}$ feet away from body. Mesh shown contains 57M cells resulting from 10 cycles of adaptive refinement.

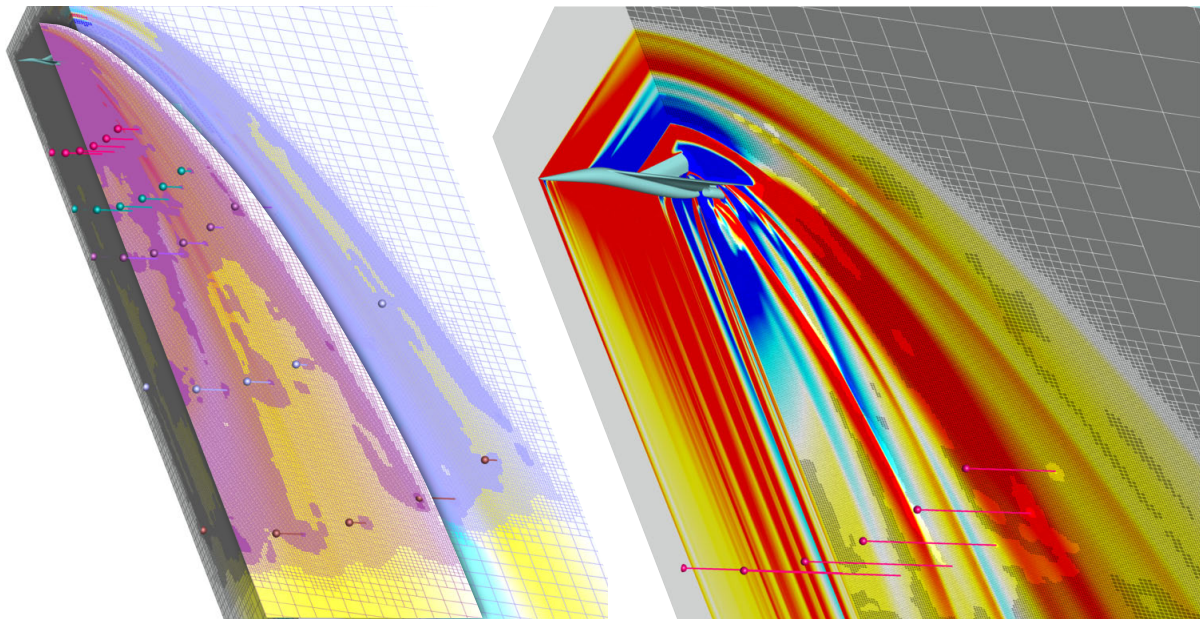


Figure 18. Case 3: Symmetry plane and cross-flow slices showing adapted Cartesian mesh and iso-bars for Lockheed Martin LM1021 configuration at $M_\infty = 1.6$, $\alpha = 2.1^\circ$. Pressure sensors shown at $\Phi = \{0^\circ, 10^\circ, 20^\circ, 30^\circ, 40^\circ, 50^\circ\}$ at distances of $h = \{1.64, 2.65, 3.50, 5.83, 8.39\}$ feet from the body. Mesh shown contains 57 M cells.

the dominant wave propagation driving the adaptation. The initial mesh had ~ 51 k cells and the mesh shown contains 57M cells after 10 cycles of adaptive refinement. As in the simpler examples presented earlier, refinement regions in Figures 17 & 18 generally track the main pressure disturbances along conic-sections that propagate toward the off-body sensors. Adaptation is also evident surrounding the sensors themselves in both the symmetry plane and crossflow cuts.

C.3. LM1021: Mesh Convergence

Results for the LM1021 configuration were submitted for the meshes shown in Figures 17 and 18 with 57M cells and 10 cycles of adaptive refinement. This relatively large case required approximately 80 GB of memory to run. Due to the larger mesh size, only one additional refinement was performed to establish mesh convergence. Figure 19 shows results for convergence of the adaptation functional (left) and convergence of the adjoint-based error estimates (right). Adaptation cycles 8–11 are labeled. As discussed earlier, convergence of the functional is a direct indication of mesh independence of the pressure signatures over the entire sensor array. Over the last 4 adaptation cycles, the corrected functional (green circles) convincingly leads the computed functional by approximately one adaptation cycle, and the correction itself vanishes

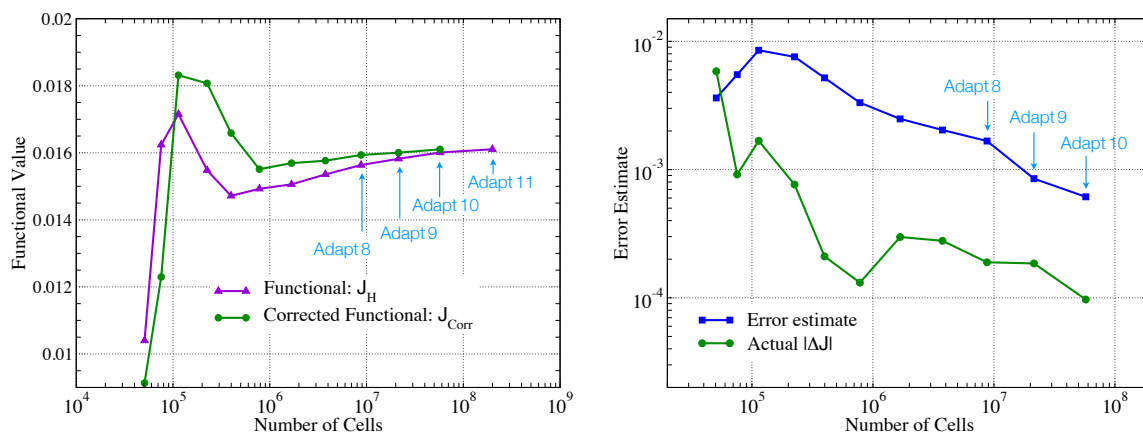


Figure 19. Mesh convergence for LM1021 case. (Left) Convergence of the functional and adjoint correction. (Right) Convergence of the adjoint-based error estimate and actual update to the functional, $|\Delta J|$.

rapidly as the mesh is refined. The frame at the right of Figure 19 shows that the estimated error-bound is also well-behaved and is everywhere conservative when compared with the actual $|\Delta\mathcal{J}|$. In this case, the actual updates are about one order of magnitude smaller than the estimate of the error-bound. The linearly decreasing error-estimate is particularly striking when considering the level of geometric and flow field complexity in this example. This smooth error convergence gives confidence not only in the extracted pressure signals, but also in the efficacy of the adjoint-driven adaptation procedure. Detailed signature convergence with mesh refinement behaves similarly to the earlier examples (*cf.* Figs. 7 & 13) and is not presented.

C.4. LM1021: Data Comparisons and Analysis

Figure 20 shows carpet plots of the pressure signatures reconstructed for each of the five values of h/L . These carpets were constructed by collecting the pressure signatures extracted at each h/L and tessellating each group in $x-\Phi$ space. This view offers a more complete understanding of the signal evolution. The figure presents these carpets from three vantage points. At the left, the perspective three-quarter view shows the scale of the actual propagation with respect to the size of the model – which is in the extreme upper left corner. Since these carpets were extracted roughly along characteristics of the Mach 1.6 flow, we can see how features in the near-field evolve as the signal propagates. The center frame shows a top view, helping to clarify the downstream extent of the propagation while offering a better view of the variation of the pressure footprint with off-track angle. At all h/L 's, the pressure signatures strengthen somewhat off-track. In addition, since the entire footprint at any intermediate h/L is completely captured by the next, this view gives insight into how the amplitude of the waves decreases as they spread away from the body. The frame at the right shows a projection in the $x-\Phi$ plane which is particularly interesting. At larger distances, the pressure field behaves as if it was generated by an equivalent slender body. The cross-flow direction essentially decouples so that propagation along any particular azimuth is independent from all others. As a result, unwrapping these carpets into $x-\Phi$ coordinates permits direct comparison of the signal's evolution along any particular off-track angle.

The symmetry plane isobars at the right of Figure 17 are helpful in tracing the source of the features shown in the carpets of Figure 20. For example, the stripe of high pressure (red) at the back of the carpets at $h=1.64, 2.65$ & 3.5 ft. clearly emanates from the sting juncture and is not generated by the model itself. More critically, we see that the main expansion (shown in blue/cyan in the middle and outboard of each carpet) deepens significantly at off-track angles greater than about 20° – despite being well controlled directly on-track ($\Phi = 0^\circ$). This strong expansion at moderate azimuth angles suggests the possibility of noisy off-track ground booms and must be examined in detail. This strong expansion persists at large h/L .

Reference [45] includes a table of all available tunnel runs relevant to the LM1021 case considered in the workshop. Figures 21 & 22 show pressure signatures from the four runs which most closely match the present conditions and signature locations. Figure 21 shows on-track ($\Phi = 0^\circ$) comparisons near $h = 1.64$ and 2.65 ft., while Figure 22 shows off-track data near $\Phi = 20^\circ$ and $\Phi = 50^\circ$. Both off-track measurements were taken at $h = 1.73$ ft., which is only about an inch farther away than the computations at 1.64 ft. Despite the slight mismatch in conditions and extraction locations, there is reasonably good agreement with the experiment for all four signatures. The comparison at the right of Figure 22 possibly shows the closest

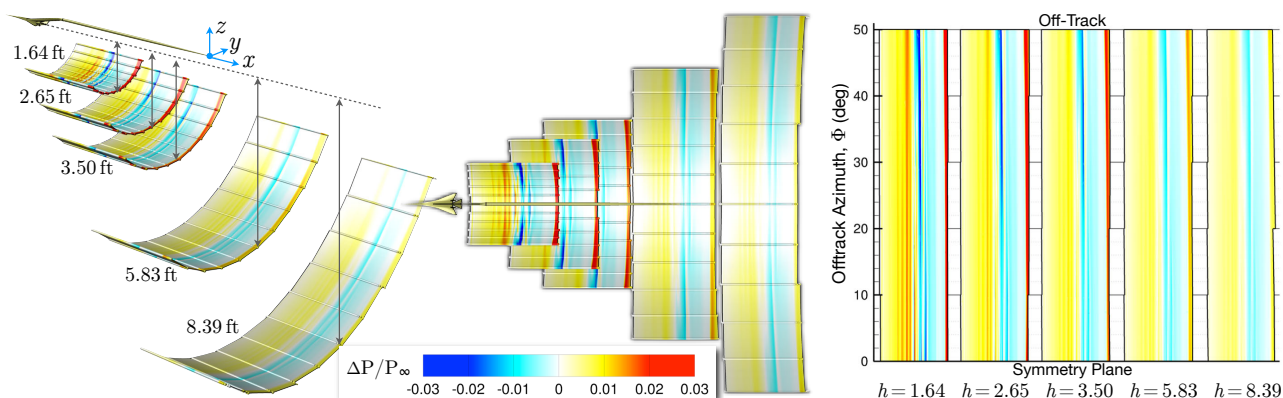


Figure 20. Near and mid-field pressure carpets for $\Phi = 0^\circ - 50^\circ$ for LM1021 configuration extracted at $h = \{1.64, 2.65, 3.50, 5.83, 8.39\}$ feet.

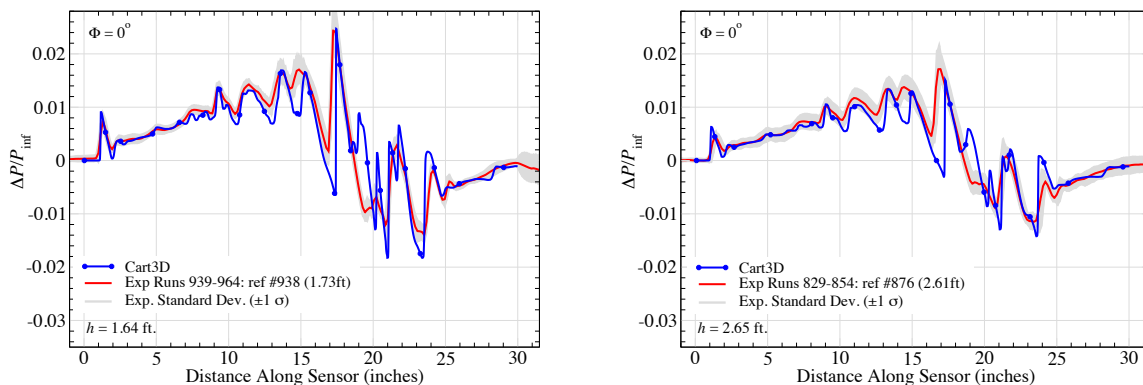


Figure 21. Comparison of on-track pressure signatures with tunnel measurements at $h = 1.64$ & 2.65 ft. Simulation results at $M_\infty = 1.6$, $\alpha = 2.1^\circ$. Experimental results with $\alpha = 2.1^\circ$ at $h = 1.73$ ft. and $\alpha = 2.3^\circ$ at $h = 2.61$ ft.

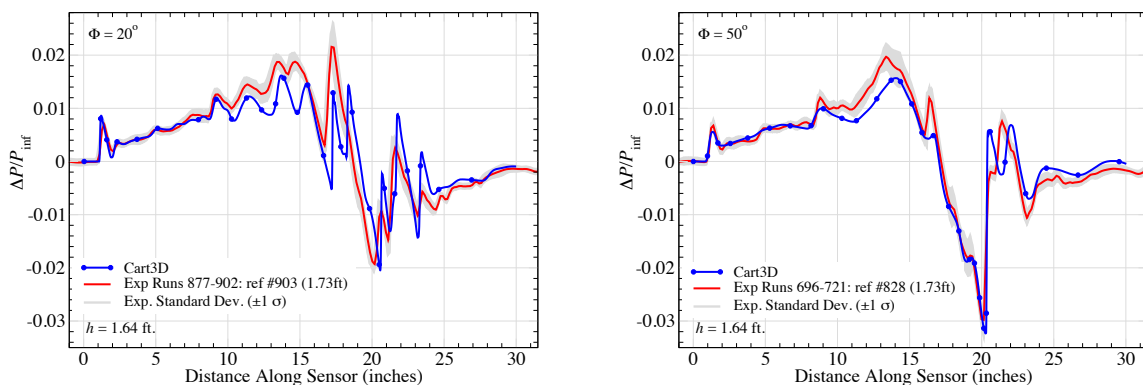


Figure 22. Comparison of off-track pressure signatures at $\Phi = 20^\circ$ & 50° with tunnel measurements. Simulation results at $M_\infty = 1.6$, $\alpha = 2.1^\circ$, at $h = 1.64$ ft. Experimental data at $\alpha = 2.3^\circ$, $h = 1.73$ ft. and $\Phi = 20^\circ$ & 47° .

agreement and is also the most striking. Experimental data for this case was taken at $\alpha = 2.3^\circ$ and $\Phi = 47^\circ$ while the simulation was at a slightly lower angle of attack ($\alpha = 2.1^\circ$) and was extracted at $\Phi = 50^\circ$. This signature is dominated by a deep expansion and relates directly to the observations about off-track behavior in the preceding paragraph. This profile is a cut through the first carpet ($h = 1.64$ ft.) in Figure 20 near the outboard edge. It quantifies the rapid transition from overpressure to deep suction discussed above which is notably stronger than even the highest peak overpressure seen at this distance; *cf.* left frame in Figure 21. The pressure carpets indicate that this expansion becomes prominent around $\Phi = 20^\circ$ and indeed, the plot at the left of Figure 22 shows the beginning of this feature at a distance of around 20 in. along the sensor. This feature would need to be propagated to the ground from one of the mid-field h/L 's to determine off-track loudness.

While agreement with measurement at all four locations in Figures 21 and 22 is reasonably good, there are some notable discrepancies through the main expansion ($x \approx 19$ in.). Given the precision of our predictions for the Seeb-ALR and the 69° delta-wing case, these differences merit closer inspection. Figure 21 shows the on-track signatures at $h = 1.64$ and 2.65 ft. In these profiles, the peak overpressure predicted by the simulations is slightly delayed as compared to the experiment. In addition, the simulations show a secondary peak, in the middle of the main expansion at $x = 19$ in., which differs from the experiment and persists out to about $\Phi = 20^\circ$. Since these results are mesh converged, its worth investigating the source of this secondary peak.

The adjoint field identifies regions of the domain responsible for particular outputs. Therefore, the adjoint solver is an excellent tool for tracing this secondary peak to its precise origin. Figure 23 outlines this investigation. We re-instrumented the mesh shown in Figure 17 using a line sensor localized to the main expansion: from about $x = 18$ in. to $x = 20$ in. We then solved the adjoint against the new functional. The resulting adjoint field highlights the particular regions of the flow and geometry responsible for just this portion of the signal. Figure 23 shows the sensor location, a view of the adjoint solution and a close-up of the geometry under wing colored by the density adjoint. The close-up shows that this portion of the main expansion is most strongly influenced by details of the underwing pressure over the front-half of the nacelle (the dark blue stripe under the wing and extending onto the nacelle itself).

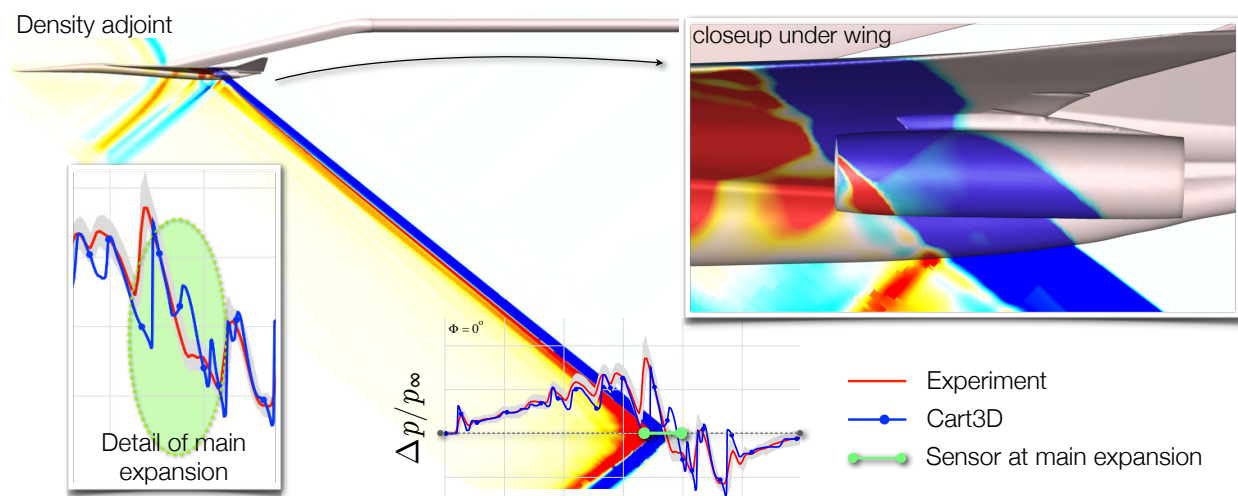


Figure 23. Adjoint investigation highlighting the region of the surface responsible for the pressure signature through the main expansion. Isobars of density adjoint. $M_\infty = 1.6$, $\alpha = 2.1^\circ$, at $\Phi = 0^\circ$.

With the source of this feature identified underwing and on the forward half of the nacelle, we can now examine local features in the pressure field and search for differences between the simulation and experiment. The tunnel tests were conducted at a Reynolds number of only 2.55 M/ft. This is approximately two orders of magnitude lower than that of the full-scale vehicle, and the low tunnel Reynolds number was a persistent concern in the test reports.^{36,41} Figure 24 shows the consequences of this low Reynolds number in the underwing region highlighted by the adjoint. The figure shows Mach and pressure contours from viscous simulations using NASA's USM3D solver and contrasts them with the inviscid simulation.ⁱ At the tunnel Reynolds number, the thick incoming boundary layer extends nearly the full height of the pylon. The Mach contours show that this viscous layer essentially fills the entire space between the wing and nacelle. As a result, the shock from the upper nacelle lip interacts strongly with this thick layer and the resulting footprint on the underwing pressure moves forward and smears out substantially. In the inviscid simulations, the upper nacelle lip throws an oblique shock that strikes the wing downstream of the inlet and reflects back down toward the sensor. There is a secondary reflection between the nacelle and lower wing surface and a strong pressure rise at the pylon leading edge. These two over-pressures propagate toward the sensor as indicated by the dashed arrows in frame (c) of Figure 24. The aft shift in the footprint of the nacelle shock and the secondary shock from the reflection and pylon directly account for the differences seen in the on-track pressure signatures in Figure 21. More recent simulations at flight Reynolds numbers show much closer agreement between inviscid and viscous results since the underwing boundary-layer is much thinner at these conditions.⁴¹

Simulation results on the 57 M cell mesh shown in Figures 17 & 18 were submitted to the workshop. This case was run on the NAS Endeavour system with 96 Intel Xeon E5-460L cores. The total memory used was under 80 GB. The total wall-clock time including initial mesh generation, all adaptation cycles and flow and adjoint solution time was about 2 hours and 20 minutes.

ⁱDetails of viscous simulations for this case with USM3D are presented in Ref. [45].

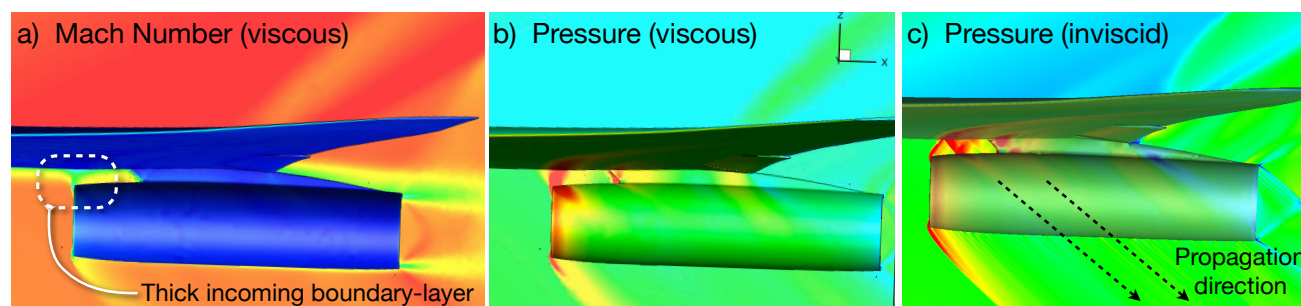


Figure 24. Comparison of the underwing region in viscous (RANS) at the wind tunnel Reynolds number with inviscid modeling. Colormaps in frames (b) and (c) are similar but not identical. $M_\infty = 1.6$, $\alpha = 2.1^\circ$. $Re_x = 2.55$ M/ft.

IV. Summary

This work presented simulation results for the First AIAA Sonic Boom Prediction Workshop using an inviscid, embedded-boundary Cartesian mesh method. The simulations used adjoint-based error estimation and adaptive meshing to automatically determine resolution required for accurate computations. Results were presented for both the mandatory and optional workshop cases. These included the Seeb-ALR body of revolution, the 69° delta-wing-body and a complete model of the Lockheed low-boom LM 1021 configuration with V-tail, three flow-through nacelles and blade-sting. In each case, we presented mesh refinement studies showing convergence of the output functional, the remaining discretization error and convergence of the pressure signals at representative sensor locations. Moreover, very good convergence of the adjoint-correction, the remaining error and the functional update were observed for all cases. Direct comparison with wind-tunnel data from the NASA Ames 9×7 ft. Supersonic Wind Tunnel provided validation of all numerical simulations. Results for all cases showed very good agreement with the available experimental data and linear theory (where appropriate).

These examples provided an opportunity to discuss various aspects of practical low-boom signature prediction. We addressed issues surrounding accurate prediction of extreme off-track pressure signatures, such as, appropriately weighting the contributions of off-track pressure sensors to the net adaptation functional and yawing the computational mesh. A heuristic weighting of pressure sensors was presented which accounts for both the reduction in signal strength with propagation distance and increased resolution requirements off-track. This weighting is designed to balance contributions to the net output functional from many individual pressure sensors. We demonstrated its effectiveness on an array of 30 sensors in simulations of the LM 1021 test case. This work also demonstrated a powerful technique for using the adjoint solver to focus on specific portions of the near-field pressure signature and tracing these directly to precise regions of the surface geometry and near-body flow. This technique allowed us to link details of the main expansion in the pressure signature to the very strong shock/boundary-layer interaction that occurs near the underwing nacelles due to the low Reynolds numbers of the experiment.

More broadly, this study showed the utility of the adaptive Cartesian mesh solver for predicting near- and mid-field pressure signatures of low-boom configurations at modest computational cost. Wall-clock times for these fully-automated solutions ranged from about an hour on a quad-core laptop, for the Seeb-ALR example, to ~ 2.5 hours on 96 cores for the LM 1021 case.

Acknowledgments

The authors wish to thank the members of the First AIAA Low Boom Workshop organizing committee for their superb effort and responsiveness throughout this work. This research was supported by the NASA Fundamental Aeronautics Program High-Speed project and by NASA Ames Research Center Contract NNA10DF26C. We are also grateful to Susan Cliff, David Rodriguez and Mathias Wintzer for many useful discussions and generously sharing their time and insights into supersonic flight and boom prediction.

References

- ¹Choi, S., Alonso, J. J., and Van der Weide, E., "Numerical and Mesh Resolution Requirements for Accurate Sonic Boom Prediction of Complete Aircraft Configurations," *AIAA Paper 2004-1060*, January 2004.
- ²Ozcer, I. A. and Kandil, O., "FUN3D/OptiGRID Coupling for Unstructured Grid Adaptation for Sonic Boom Problems," *AIAA Paper 2008-0061*, January 2008.
- ³Nemec, M., Aftosmis, M. J., and Wintzer, M., "Adjoint-Based Adaptive Mesh Refinement for Complex Geometries," *AIAA Paper 2008-0725*, January 2008.
- ⁴Wintzer, M., Nemec, M., and Aftosmis, M. J., "Adjoint-Based Adaptive Mesh Renement for Sonic Boom Prediction," *AIAA Paper 2008-6593*, August 2008.
- ⁵Howe, D. C., "Hybrid Cart3D/OVERFLOW Near-Field Analysis of a Low Boom Configuration with Wind Tunnel Comparisons," *AIAA Paper 2011-3336*, June 2011.
- ⁶Park, M. A., "Low Boom Configuration Analysis with FUN3D Adjoint Simulation Framework," *AIAA Paper 2011-3337*, June 2011.
- ⁷Cliff, S. E., Elmiligui, A. A., Campbell, R., and Thomas, S. D., "Evaluation of Refined Tetrahedral Meshes with Projected, Stretched, and Sheared Prism Layers for Sonic Boom Analysis," *AIAA Paper 2011-3338*, June 2011.
- ⁸Nemec, M. and Aftosmis, M. J., "Parallel Adjoint Framework for Aerodynamic Shape Optimization of Component-Based Geometry," *AIAA Paper 2011-1249*, January 2011.

- ⁹Carter, M. B., Campbell, R., and Nayani, S., "USM3D Analysis of a Low Boom Configuration," *AIAA Paper 2011-3335*, June 2011.
- ¹⁰Alauzet, F. and Loseille, A., "High-Order Sonic Boom Modeling Based on Adaptive Methods," *Journal of Computational Physics*, Vol. 229, No. 3, 2010, pp. 561-593.
- ¹¹Cliff, S. E., Thomas, S. D., McMullen, M., Melton, J. E., and Durston, D. A., "Assessment of Unstructured Euler Methods for Sonic Boom Pressure Signatures Using Grid Refinement and Domain Rotation Methods," NASA/TM 2008-214568, NASA, September 2008.
- ¹²Thomas, C., "Extrapolation of Sonic Boom Pressure Signatures by the Waveform Parameter Method," NASA TN-D-6832, June 1972.
- ¹³Durston, D. A., "A Preliminary Evaluation of Sonic Boom Extrapolation and Loudness Calculation Methods," *High-Speed Research: Sonic Boom*, NASA CP 10133, NASA Ames Research Center, May 12-14 1993, pp. 301-323.
- ¹⁴Rallabhandi, S. K., "Advanced Sonic Boom Prediction Using Augmented Burger's Equation," *AIAA Paper 2011-1278*, January 2011.
- ¹⁵Campbell, R., Carter, M. B., Deere, M., and Waithe, K. A., "Efficient Unstructured Grid Adaptation Methods for Sonic Boom Prediction," *AIAA Paper 2008-7327*, June 2008.
- ¹⁶Jones, W. T., Nielsen, E. J., and Park, M. A., "Validation of 3D Adjoint Based Error Estimation and Mesh Adaptation for Sonic Boom Prediction," *AIAA Paper 2006-1150*, Jan 2006.
- ¹⁷Kandil, O. and Ozer, I. A., "Sonic Boom Computations for Double-Cone Configuration using CFL3D, FUN3D and Full-Potential Codes," *AIAA Paper 2006-0414*, January 2006.
- ¹⁸Alauzet, F., Dervieux, A., and Loseille, A., "Fully Anisotropic Goal-Oriented Mesh Adaptation for 3D Steady Euler Equations," *Journal of Computational Physics*, Vol. 229, No. 8, 2010, pp. 2866-2897.
- ¹⁹Waithe, K. A., "Introduction to the First Low Boom Prediction Workshop," *AIAA Paper 2013-0650*, Jan. 2013.
- ²⁰Park, M. A., Aftosmis, M. J., Campbell, R. L., Carter, M. B., Cliff, S. E., and Bangert, L. S., "Summary of the 2008 NASA Fundamental Aeronautics Program Sonic Boom Prediction Workshop," *AIAA Paper 2013-0649*, Jan. 2013.
- ²¹Aftosmis, M. J. and Berger, M. J., "Multilevel Error Estimation and Adaptive h -Refinement for Cartesian Meshes with Embedded Boundaries," *AIAA Paper 2002-0863*, Reno, NV, Jan. 2002.
- ²²Nemec, M., Aftosmis, M. J., Murman, S. M., and Pulliam, T. H., "Adjoint Formulation for an Embedded-Boundary Cartesian Method," *AIAA Paper 2005-0877*, Reno, NV, Jan. 2005.
- ²³Aftosmis, M. J., Berger, M. J., and Melton, J. E., "Robust and Efficient Cartesian Mesh Generation for Component-Based Geometry," *AIAA Journal*, Vol. 36, No. 6, June 1998, pp. 952-960.
- ²⁴van Leer, B., "Flux-Vector Splitting for the Euler Equations," ICASE Report 82-30, Sept. 1982.
- ²⁵Aftosmis, M. J., Berger, M. J., and Adomavicius, G. D., "A Parallel Multilevel Method for Adaptively Refined Cartesian Grids with Embedded Boundaries," *AIAA-Paper 2000-0808*, Jan. 2000.
- ²⁶Aftosmis, M. J., Berger, M. J., and Murman, S. M., "Applications of Space-Filling-Curves to Cartesian methods in CFD," *AIAA-Paper 2004-1232*, Jan. 2004.
- ²⁷Berger, M. J., Aftosmis, M. J., and Murman, S. M., "Analysis of Slope Limiters on Irregular Grids," *AIAA Paper 2005-0490*, Jan. 2005.
- ²⁸Nemec, M. and Aftosmis, M. J., "Adjoint Sensitivity Computations for an Embedded-Boundary Cartesian Mesh Method," *Journal of Computational Physics*, Vol. 227, 2008, pp. 2724-2742.
- ²⁹Nemec, M. and Aftosmis, M. J., "Adjoint Error-Estimation and Adaptive Refinement for Embedded-Boundary Cartesian Meshes," *AIAA Paper 2007-4187*, June 2007.
- ³⁰Venditti, D. A. and Darmofal, D. L., "Grid Adaptation for Functional Outputs: Application to Two-Dimensional Inviscid Flow," *Journal of Computational Physics*, Vol. 176, 2002, pp. 40-69.
- ³¹Becker, R. and Rannacher, R., "An Optimal Control Approach to a Posteriori Error Estimation in Finite Element Methods," *Acta Numerica 2000*, 2001, pp. 1-102.
- ³²Giles, M. B. and Pierce, N. A., "Adjoint error correction for integral outputs," *Error Estimation and Adaptive Discretization Methods in Computational Fluid Dynamics*, edited by T. Barth and H. Deconinck, Vol. 25 of *Lecture Notes in Computational Science and Engineering*, Springer-Verlag, 2002.
- ³³Barth, T., "Numerical Methods and Error Estimation for Conservation Laws on Structured and Unstructured Meshes," Lecture notes, von Karman Institute for Fluid Dynamics, Series: 2003-04, Brussels, Belgium, March 2003.
- ³⁴Huntton, L. W., Hicks, R. M., and Mendoza, J. P., "Some Effects of Wing Planform on Sonic Boom," NASA TN-D-7160, National Aeronautics and Space Administration, January 1973.
- ³⁵Cliff, S. E., Elmiligui, A. A., Aftosmis, M. J., Thomas, S. D., Morgenstern, J. M., and Durston, D. A., "Design and Evaluation of a Pressure Rail for Sonic Boom Measurement in Wind Tunnels," *Seventh International Conference on Computational Fluid Dynamics (ICCFD7)*, Paper ICCFD7-2006, Big Island, Hawaii, June 2012.
- ³⁶Morgenstern, J. M., "How to Accurately Measure Low Sonic Boom or Model Surface Pressures in Supersonic Wind Tunnels," *AIAA Paper 2012-3215*, June 2012.
- ³⁷Morgenstern, J. M., Buonanno, M., and Marconi, F., "Full Configuration Low Boom Model and Grids for 2014 Sonic Boom Prediction Workshop," *AIAA Paper 2013-0647*, Jan. 2013.
- ³⁸Morgenstern, J., Norstrud, N., Sokhey, J., Martens, S., and Alonso, J. J., "Advanced Concept Studies for Supersonic Commercial Transports Entering Service in the 2018 to 2020 Period," NASA CR-2013-217820, NASA Langley Research Center, Feb. 2013.
- ³⁹Darden, C. M., "Sonic Boom Minimization with Nose-Bluntness," NASA-TP 1348, National Aeronautics and Space Administration, 1979.
- ⁴⁰George, A. R. and Seabass, R., "Sonic Boom Minimization Including Both Front and Rear Shocks," *AIAA Journal*, Vol. 9, No. 10, 1971, pp. 2091-2093.

⁴¹Cliff, S. E., Durston, D. A., and Elmiligui, A. A., “Experimental and Computational Sonic Boom Assessment of Lockheed Martin N+2 Phase I and II Low Boom Models,” NASA-TP 2013-XXXX, National Aeronautics and Space Administration, Ames Research Center, Moffett Field, CA 94035-1000, October 2013.

⁴²Cliff, S. E. and Thomas, S. D., “Euler/Experiment Correlations of Sonic Boom Pressure Signatures,” *Journal of Aircraft*, Vol. 30, No. 5, Sept.-Oct. 1993.

⁴³Park, M. A. and Darmofal, D. L., “Output-Adaptive Tetrahedral Cut-Cell Validation for Sonic Boom Prediction,” *AIAA Paper 2008-6595*, August 2008.

⁴⁴Aftosmis, M. J., Nemec, M., and Cliff, S. E., “Adjoint-Based Low-Boom Design with Cart3D,” *AIAA Paper 2011-3500*, June 2011.

⁴⁵Cliff, S. E., Durston, D. A., Elmiligui, A. A., Jensen, J. C., and Chan, W. M., “Computational and Experimental Assessment of Models for the First AIAA Sonic Boom Prediction Workshop,” *AIAA Paper 2014-XXXX*, Jan. 2014.